KURENAI
Kyoto University Research Information Repository

KYOTO UNIVERSITY

Title	Effect of Fe content on physical properties of BaO–CeOx–FeOy catalysts for direct NO decomposition
Author(s)	Hong, Won-Jong; Ueda, Mao; Iwamoto, Shinji; Hosokawa, Saburo; Wada, Kenji; Kanai, Hiroyoshi; Deguchi, Hiroshi; Inoue, Masashi
Citation	Applied Catalysis B: Environmental (2011), 106(1-2): 142-148
Issue Date	2011-07
URL	http://hdl.handle.net/2433/147066
Right	© 2011 Elsevier B.V.
Type	Journal Article
Textversion	author

Kyoto University

Effect of Fe content on physical properties of BaO–CeO$_x$–FeO$_y$ catalysts for direct NO decomposition

Won-Jong Hong [a], Mao Ueda [a], Shinji Iwamoto [b], Saburo Hosokawa [a],

Kenji Wada [a], Hiroyoshi Kanai [a], Hiroshi Deguchi [c], Masashi Inoue [a,*]

[a] Department of Energy and Hydrocarbon Chemistry

Graduate School of Engineering, Kyoto University, Katsura, Kyoto, 615-8510, JAPAN

[b] Department of Chemistry and Chemical Biology,

Graduate School of Engineering, Gunma University, Tenjin, Kiryu 376-8515, JAPAN

[c] Power Engineering R&D Center, The Kansai Electric Power Company,

Inc., 3-11-20, Nakoji, Amagasaki 661-0974, JAPAN

[*] Corresponding author

Tel.: +81-75-383-2478

fax: +81-75-383-2479.

E-mail address: inoue@scl.kyoto-u.ac.jp (M. Inoue)

ABSTRACT

The physical properties of the Ba-loaded Ce–Fe mixed oxide catalysts, which exhibited high activity for NO decomposition to N_2, were investigated. The optimum Fe/(Ce+Fe) molar ratio was 0.02. The X-ray absorption near edge structure, electron spin resonance, and diffuse reflectance UV–visible spectra indicated that the optimum catalyst had the highest proportion of isolated tetrahedral Fe^{3+} ions in all the Fe species. Raman spectra suggested that incorporation of Fe^{3+} in the fluorite structure of CeO_2 caused an increase in the concentration of oxygen vacancies, which play an important role in the NO decomposition activity of the catalysts. Temperature-programmed desorption (TPD) of O_2 showed that the addition of the Fe component to BaO/CeO_2 enhanced O_2 uptakes and facilitated oxygen desorption. NO-TPD profiles showed that NO desorption was associated with the desorption of O_2, indicating that these two species are formed by decomposition of surface nitrate species.

Keywords: Ce–Fe mixed oxide, Oxygen vacancy, O_2-TPD, NO-TPD, NO decomposition

1. Introduction

Cerium oxide and CeO_2-containing materials have attracted much attention as catalysts or structural and electronic promoters for catalysts [1]. Some cerium–transition metal mixed oxides have a large number of surface and bulk oxygen vacancies, improving oxygen storage capacity, and exhibit favorable redox properties. Among many cerium-based mixed oxide systems, Fe–Ce mixed oxides have attracted attention. They have also been investigated as the catalysts for wet air oxidation of p-coumaric acid [2], synthesis of 3-pentanone from 1-propanol [3], and Fischer-Tropsch synthesis [4, 5].

Hrovat et al. prepared Fe–Ce mixed oxide by solid state reaction of Fe_2O_3, and CeO_2 at 1,200 ºC, but no indication of the dissolution of Fe in the ceria lattice was found [6]. However, Li et al. successfully synthesized $Ce_{1-x}Fe_xO_2$ solid solutions by the hydrothermal method and found the sample had extremely low concentration of oxygen vacancies. Since no Ce^{3+} ions were detected in the samples, they attributed this result to the distribution of Fe^{3+} ions at Ce^{4+} sites and interstitial sites in a ratio of ca. 3:1 [7].

Since emission of nitrogen oxides (NO_x) causes severe environmental problems, effective methods to detoxify NO_x in emission gases have been investigated. Several practical NO_x emission control technologies such as three-way catalysts for gasoline-fueled vehicles, NO_x storage–reduction (NSR) systems for lean-burn engines,

and selective catalytic reduction (SCR) processes for large-scale combustion facilities are now applied; however, there is still a great research interest for the development of novel and more efficient de-NO_x methods. Among various de-NO_x strategies, direct decomposition of NO (NO $\rightarrow$ 1/2O_2 + 1/2N_2) is most desirable because this reaction is thermodynamically favorable at lower temperatures and does not need any reductants such as NH_3, H_2, CO, or hydrocarbons.

Various catalysts have been found to be effective for direct decomposition of NO [8-20]. As for perovskite-type oxides and C-type cubic rare earth oxides, high activities of these catalysts were attributed to the oxide ion vacancies in the catalysts [14-19].

Previously, we examined the performance of Ba catalysts supported on Co_3O_4 and CeO_2, and it was found that the NO conversion was correlated to the number of basic sites [21]. The effect of the addition of second components to CeO_2 was examined, and it was found that Ba catalysts supported on Ce–Mn mixed oxides showed significantly improved activities for direct decomposition of NO [22]. In the previous paper, we examined the direct decomposition of NO over Ba catalysts supported on Ce–Fe mixed oxides and found that the catalysts with the Fe/(Ce+Fe) ratio of 0.02 exhibited quite high activities [23]. In this study, Ba-loaded Ce–Fe mixed oxides were characterized, and the correlation between the properties of the catalysts and their NO decomposition

activities was discussed. The mechanisms for the direct NO decomposition on this catalyst are also discussed.

2. Experimental

2.1. Preparation of the catalysts

Ce–Fe mixed oxide samples (designated as Ce–Fe(x), x = Fe/(Ce+Fe) molar ratio) were prepared by the glycothermal method [23]. Appropriate amounts of $Ce(CH_3COO)_3 \cdot H_2O$ (Wako) and $Fe(CH_3COO)_2$ (Wako; total amount of Ce and Fe was 50 mmol) were suspended in 100 ml of 1,4-butanediol (Nacalai), and this mixture was set in a 300-ml autoclave. After the atmosphere inside the autoclave was completely replaced with nitrogen, the autoclave was heated to 300 °C at a rate of 2.3 °C·min^{-1} and kept at that temperature for 2 h. After cooling, the resultant powder product was collected by centrifugation, washed with acetone repeatedly, air-dried, and calcined at 400 °C in air for 4 h.

Barium oxide was loaded on Ce–Fe(x) by an impregnation method using an aqueous solution of barium nitrate (Wako), followed by calcination at 800 °C for 1 h. The barium loading (as BaO) was adjusted to 7 wt% [23]. These catalysts were designated as BaO/Ce–Fe(x).

2.2. Direct NO decomposition

Catalytic tests for the NO decomposition reaction were carried out in a fixed-bed flow reactor of quartz glass tubing with an inner diameter of 10 mm. The catalyst (0.50 g), after pressed into a pellet and pulverized into 10–22 mesh size, was placed in the reactor. The catalyst bed was heated to 550 °C in a helium flow and held at that temperature for 30 min. Then, the reaction gas composed of 6,000 ppm NO and helium balance was introduced to the catalyst bed at 30 ml·min^{-1} (W/F = 1.0 g·s·ml^{-1}). The reaction temperature was increased from 550 to 800 °C at 5 °C·min^{-1} and kept for 15 min at every 50 °C interval to attain the steady state. The effluent gas was analyzed using a gas chromatograph (GL Science, MicroGC 2002) equipped with Molsieve 5A and Poraplot Q columns. The NO conversion is expressed on the basis of the formation of N_2:

$$\text{NO conversion} = \frac{2[N_2]_{out}}{[NO]_{in}},$$

where $[N_2]_{out}$ and $[NO]_{in}$ are the N_2 concentration in the exhaust and the NO concentration in the feed, respectively.

In the present study, the concentrations of N_2O formed as a by-product were less than 50 ppm.

2.3. Characterization of the catalysts

6

The bulk Fe/(Ce+Fe) ratios were determined with a Shimadzu ICPS-1000IV inductively coupled plasma atomic emission spectrometer (ICP-AES). The catalysts were dissolved in phosphoric acid at 80 °C and then the solutions were diluted to about 0.2 g·l^{-1} concentration with water. The surface Fe/(Ce+Fe) and Ba/(Ce+Fe+Ba) ratios were determined with an ULVAC-PHI 5500 X-ray photoelectron spectrometer (XPS) with a hemispherical energy analyzer. Samples were mounted on an indium foil, and then transferred to the XPS analyzer chamber. The residual gas pressure in the chamber during data acquisition was less than 1×10^{-8} Torr (1 Torr = 133.3 N·m^{-2}). The spectra were measured at room temperature using Mg Kα radiation (15 kV, 400 W).

X-ray absorption near edge structure (XANES) measurements were performed at the beamline BL16B2 in the SPring-8 synchrotron radiation research facility. X-ray from the storage ring was monochromatized using a Si(111) crystal monochromator. The intensity of fluorescence X-ray from the sample was detected using a silicon drift detector (SDD) with 19 elements. The proportions of tetrahedral iron in the samples were estimated by the linear combination fitting (LCF) method from their XANES data. As the tetrahedral Fe^{3+} and octahedral Fe^{3+} standards, FePO$_4$ and α-Fe$_2$O$_3$ were used, respectively.

Electron spin resonance (ESR) spectra were recorded with a JEOL JES-SRE2X

spectrometer at −196 ℃. The *g*-factors were determined by using an Mn^{2+} marker doped in MgO.

Raman spectra were recorded on a Jobin-Yvon T64000 Raman spectrometer at room temperature using a 514.5 nm argon laser beam.

Diffuse reflectance UV−visible spectroscopy (UV−vis) was carried out with a JASCO V-650 spectrometer at room temperature. The UV−vis absorption spectrum of $BaSO_4$ packed in a quartz cell was used as the background spectrum, and spectra of the samples were expressed using the Kubelka−Munk function. The UV−vis spectra of Fe species were determined by subtracting the spectrum of the CeO_2 from the observed spectra for Ce−Fe(*x*) and deconvoluted into bands by fitting the Gaussian peak profiles.

Temperature-programmed desorption of O_2 or NO (O_2-TPD or NO-TPD) was carried out in the fixed-bed flow reactor. For the O_2-TPD, the catalyst was heated at 550 °C for 30 min in He and cooled to 50 °C, and a gas composed of 20 % O_2 and He balance was allowed to flow over the catalyst at W/F = 1.0 g·s·ml^{-1} for 1 h. After the excess adsorptive gas was purged with a He flow, the catalyst was heated to 800 °C at a rate of 10 °C·min^{-1} in the He flow. For the NO-TPD, a gas composed of 6,000 ppm NO and He balance was allowed to flow over the catalyst at 550 °C for 1 h. After the excess adsorptive gas was purged with a He flow, the catalyst was cooled to 100 °C and then

was heated to 800 °C at a rate of 10 °C·min^{-1} in the He flow. The desorbed species were analyzed with a Pfeiffer Vacuum Omnistar GSD 301 O 1 Q-MASS spectrometer.

3. Results and discussion

3.1. Composition of the BaO/Ce–Fe(x) catalyst

The bulk and surface compositions of the BaO/Ce–Fe(x) catalysts were investigated by the ICP and XPS analyses, and the results are summarized in Table 1. The ICP analysis showed that the catalysts had almost the same Fe contents as the starting compositions for the glycothermal reaction. On the other hand, the XPS results indicated that for the BaO/Ce–Fe(x) catalysts with small Fe contents (x < 0.17), Fe components were enriched on the surface region of the catalyst, whereas the catalyst with a high Fe content (x = 0.5) had a surface composition essentially identical with the bulk composition. As for the surface Ba content, the BaO/Ce–Fe(x) catalysts with x < 0.17 had the surface Ba ratios higher than those of the catalysts with x = 0.17 and 0.5, indicating that the high dispersion of Ba species is attained on the surface of the catalysts with low Fe contents.

3.2. Fe K-edge XANES spectra of the BaO/Ce–Fe(x) catalysts

The coordination structure of iron species was investigated by the X-ray absorption near edge structure (XANES) technique, which is a reliable method to elucidate the coordination structure of iron [24-26]. The Fe K-edge XANES spectra of the BaO/Ce–Fe(x) catalysts are shown in Fig. 1 together with those of $FePO_4$ (tetrahedral Fe^{3+}) and α-Fe_2O_3 (octahedral Fe^{3+}) references. The most striking feature of the spectra of the catalysts is that a clear pre-edge peak was observed at ~7111 eV, and relative intensity of the pre-edge peak increased with the decrease in the Fe content. Because the transition of 1s electron to 3d orbitals is forbidden, the pre-edge peak is caused by the transition of 1s electron to 3d orbitals mixed with 4p orbitals [27, 28]. Therefore, the central iron deviates from the centrosymmetrical environment. Since the tetrahedral structure does not have the inversion symmetry, the appearance of the pre-edge peak suggests that Fe species in the catalysts with low Fe contents possess the tetrahedral Fe^{3+} structure.

In the main edge region, the spectra of the reference samples (Figs. 1(h) and 1(g)) exhibited an absorption peak at 7127 eV (α peak) due to tetrahedral Fe^{3+} or a peak at 7130 eV (β peak) due to the octahedral Fe^{3+}. The XANES spectra of the catalysts with high Fe contents ($x \geq 0.17$) (Fig. 1(d), (e), and (f)) are similar to that of α-Fe_2O_3 and exhibited a strong absorption peak at 7130 eV (β peak), indicating that Fe species in

10

these catalysts have the octahedral structure. For the catalysts with small amounts of Fe ($x < 0.17$) (Fig. 1(a), (b), and (c)), however, XANES spectra showed the α peak, indicating that these catalysts contained tetrahedral Fe^{3+} ions predominantly.

The XANES spectra of the catalysts were well simulated by the linear combination of the spectra of the reference samples with tetrahedral and octahedral Fe^{3+} ions; therefore, the possibility that Fe ions in the catalysts have unusual coordination structure such as penta-coordinated structure can be ruled out. The proportions of tetrahedral Fe^{3+} ions in the catalysts were calculated by the LCF method on the basis of the spectra of the reference samples. The calculated tetrahedral Fe^{3+} proportions of the BaO/Ce–Fe(x) catalysts are shown in Fig. 2. For comparison, the NO conversion at 800 ℃ is also plotted in the figure. The maximum tetrahedral Fe^{3+} proportion was attained for the sample with $x = 0.02$, and further increase in the Fe content decreased the tetrahedral Fe^{3+} proportion. This tendency is similar to the effect of Fe on the NO decomposition activity. These results suggest that the local structure of Fe^{3+} is one of the important factors for the catalytic activity.

Mole of NO converted at 600 ℃ (The data at this reaction temperature were taken because NO conversions were relatively low) per mole of tetrahedral Fe^{3+} in the catalyst was calculated, and the results are also shown in Fig. 2. Although the data were slightly

11

scattered, the NO decomposition activity normalized by the tetrahedral Fe^{3+} gradually

decreased with the increase in Fe content in the catalyst, indicating that the proportion

of the tetrahedral Fe^{3+} ions that did not contribute to the NO decomposition activity

increased with the increase in Fe content.

3.3. ESR spectra of the BaO/Ce–Fe(x) catalysts

Fig. 3 shows the ESR spectra of the BaO/Ce–Fe(x) catalysts. Weak signals at $g \approx 1.96$,

and 1.94 [29, 30] are attributed to Ce^{3+} ions, indicating that Ce-rich catalysts ($x \leq$

0.048) contain small amounts of Ce^{3+} ions (Fig. 3A). Except for these catalysts, the

characteristic signals due to Ce^{3+} were not observed. Since clustered iron oxide and

oxyhydroxide phases exhibit a broad signal in a 150–400 mT range centered at $g \approx$

2.2–2.6 [31-33], as is evident for the spectrum of α-Fe_2O_3 (Fig. 3(h)), the broad signals

observed for the samples with $x = 0.17$ ($g = 2.6$) and 1.0 ($g = 2.4$) are attributed to bulk

Fe^{3+} species. The signal (Fig. 3B) at $g \approx 2.0$ was assigned to isolated octahedral Fe^{3+}

species [32, 34] or iron oxide clusters [35, 36].

The signal (Fig. 3C) at $g \approx 4.3$ has been assigned to isolated Fe^{3+} species with either

tetrahedral [32-34, 37] or octahedral [32, 33, 35, 37] structure, and it is known that just

from the signal position alone it is not possible to conclude whether the respective Fe

ions are octahedrally or tetrahedrally coordinated [33, 34, 36]. However, since this signal is significant in the spectra of the catalysts with low Fe contents, we assigned the ESR signal at $g \approx 4.3$ to the tetrahedrally coordinated Fe^{3+} species, because the result of the XANES analysis confirmed the presence of tetrahedrally coordinated Fe^{3+} species in these catalysts.

As shown in Fig. 3, the ESR signal at $g \approx 4.3$ had the highest intensity for the BaO/Ce–Fe(0.02) catalyst. This result accords with the result obtained from the XANES spectra, which indicate that the BaO/Ce–Fe(0.02) catalyst had the highest proportion of the tetrahedral Fe^{3+} ions. However, the data plotted in Fig. 2 are not "contents" but "proportion," and the highest tetrahedral content was attained by the catalyst with $x = 0.17$ because this catalyst contains a large amount of Fe^{3+}. This argument indicates the catalysts with large Fe contents have tetrahedral Fe^{3+} ions that do not give the ESR signal at $g = 4.3$.

3.4. UV–vis spectra of the BaO/Ce–Fe(x) catalysts

UV–vis spectra of the BaO/Ce–Fe(x) catalysts are shown in Fig. 4. The shapes of the spectra, which varied remarkably with the Fe content, can be represented by the combination of sub-bands as shown in the figure. For the catalyst with a low Fe content

($x = 0.01$), essentially no absorption was observed at >400 nm, and 100% of the spectral

area is accounted for by sub-bands centered at <400 nm. With increasing the Fe content,

the spectrum becomes broader, and 95% of the spectral area is covered by the bands

centered at >300 nm.

The assignment of the sub-bands has been discussed in detail in literature [34, 38-40].

On the basis of these reports, we ascribe the bands at ~220 nm and ~285 nm to the Fe^{3+}

← O charge transfer bands of isolated Fe ions. The band at ~350 nm was assigned to

$Fe_x^{3+}O_y$ oligomeric clusters, and sub-bands at >400 nm, to large Fe_2O_3 particles. Table 2

summarized the relative areas of the sub-bands. Since the absorbance of each band is

not known, the data cannot be translated into the relative content of each Fe species.

However, variation of the area of each band may be discussed. The BaO/Ce–Fe(0.02)

catalyst had the highest relative area of the band due to the isolated Fe^{3+} species, and the

area of this band decreased by the further increase in the Fe content. This result is in

good agreement with the result obtained from the XANES spectra.

3.5. Raman spectra of the BaO/Ce–Fe(x) catalysts

The Raman spectra of CeO_2 and BaO/Ce–Fe(x) catalysts both calcined at 800 °C are

shown in Fig. 5A. The Raman peak of the CeO_2 sample due to F_{2g} active mode was

observed at 463.5 cm^{-1} [41-43]. The Raman spectrum of the BaO/Ce–Fe(0) (BaO/CeO$_2$) (Fig. 5A(h)) was similar to that of CeO$_2$ (Fig. 5A(i)). For the Fe-containing samples ($x >$ 0), however, a significant peak shift to lower wavenumber and broadening of the peak due to F_{2g} mode of CeO$_2$ were recognized. These results indicate that Fe ions are incorporated in the CeO$_2$ matrix.

For Fe-rich catalysts ($x =$ 1.0 and 0.5) (Fig. 5A(b and c)), Raman shifts were also observed at 222, 243, 290, 406, 495, and 607 cm^{-1} due to α-Fe$_2$O$_3$ (Fig. 5A(a)), and at 683 cm^{-1} due to the BaFe$_{12}$O$_{19}$ phase [44]. While the α-Fe$_2$O$_3$ phase has been detected by the XRD analysis, the latter phase was not detected [23], suggesting that it was highly dispersed on the catalyst surface.

For all the samples, broad Raman peaks were observed at ~256 and ~582 cm^{-1} (Fig. 5B), which were attributed to the defect space including an O^{2-} vacancy [45]. However, the peak at ~582 cm^{-1} may overlap with the relatively broad peak at 607 cm^{-1} due to the α-Fe$_2$O$_3$ phase, and the intensity of the ~582 cm^{-1} peak increased with increasing the Fe content. Consequently, the Raman peak at ~256 cm^{-1} of the BaO/Ce–Fe(x) catalysts is attributed exclusively to the oxygen vacancy. The ratio of the intensity of the peak at ~256 cm^{-1} to that of the peak due to CeO$_2$ at ~460 cm^{-1} (denoted as I_{256}/I_{460}) indicates the relative content of oxygen vacancies in the solid solution. Fig. 6 shows the effect of

the Fe content on the I_{256}/I_{460} values for BaO/Ce–Fe(x). The addition of small amounts

of Fe significantly increased the concentration of oxygen vacancies. The largest I_{256}/I_{460}

value was attained for $x = 0.02$, and further increase in the Fe content rather decreased

the concentration of oxygen vacancies. The I_{256}/I_{460} profile is quite similar to that shown

in Fig. 2. Therefore, the I_{256}/I_{460} value was plotted against the proportion of tetrahedral

Fe^{3+} determined by the XANES spectrum. As shown in the inset of Fig. 6, linear

correlation was obtained, although the data are slightly scattered. This result indicates

that incorporation of tetrahedral Fe^{3+} ions in the CeO_2 matrix is the origin for the

formation of oxygen vacancies in the CeO_2 matrix. However, as discussed in section 3.3,

"concentration" is plotted against "proportion" in the inset. The observed linear

correlation suggests that a part of tetrahedral Fe^{3+} ions do not contribute to the

formation of the oxygen vacancies, and that the proportion of such tetrahedral Fe^{3+} ions

in total tetrahedral Fe^{3+} ions increases with the increase in the Fe content. This argument

accords with those given in sections 3.2 and 3.3; that is, the catalyst with large Fe

contents have tetrahedral Fe^{3+} ions which do not give the ESR signal at $g = 4.3$ nor

contribute to the NO decomposition activity. Therefore, such tetrahedral Fe^{3+} ions do

not contribute to the formation of the oxygen vacancies. No direct information was

available for the Fe species containing such tetrahedral Fe^{3+} ions. One possible

16

explanation is the formation of highly dispersed $BaFe_2O_4$ phase. This phase was reported to possess tetrahedral Fe^{3+} ions [46, 47] and to be formed easily by the reaction of BaO and Fe_3O_3 [48, 49].

If one assumes that Fe^{3+} ions occupy the Ce^{4+} sites, oxygen vacancies would be formed to compensate the charge imbalance. However, the fluorite structure of CeO_2 forms a primitive cubic sublattice of oxygen atoms, and therefore tetrahedral Fe^{3+} ions cannot be accommodated in this oxygen sublattice. Therefore, we conclude that tetrahedral Fe^{3+} ions are located in the defect or surface sites of CeO_2.

In a previous work [50], we found that Mn^{2+} ions are located in the Ce^{4+} sites of the fluorite structure of CeO_2 increasing the concentration of oxygen vacancies. The maximum oxygen vacancy concentration was found for the sample with Mn/(Ce+Mn) = 0.25. In the present case, on the contrary, the maximum oxygen vacancy concentration was attained for the sample with Fe/(Ce+Fe) = 0.02. Therefore, only a limited amount of Fe^{3+} ($x \leq 0.02$) can contribute to the formation of oxygen vacancies. This is because only a limited number of defect (or surface) sites that can accommodate the tetrahedral Fe^{3+} ions are available for the CeO_2 particles. These results accord with the result reported by Peŕez-Alonso et al. who showed that the iron-rich Fe–Ce solid solutions with the fluorite structure are hardly formed by high temperature calcination (>500 ℃)

17

[5]. Excess Fe^{3+} ions are located in interstitial sites, which decrease the oxygen vacancy concentration.

In the previous paper [50], we showed that the concentration of oxygen vacancies in BaO/Ce–Mn catalyst plays an important role in deriving NO decomposition activity of the catalysts. Fig. 7 shows the correlation between NO conversion at 800 ºC and the I_{256}/I_{460} value calculated from the Raman spectra of the BaO/Ce–Fe(x) (present study) and BaO/Ce–Mn(x) [50]. With increasing I_{256}/I_{460}, NO decomposition activity of the catalysts increased irrespective of the modifier for CeO_2. Therefore, chemical nature of the modifier does not affect the catalyst activity but oxygen vacancy formed by the modifier plays a very important role for the direct decomposition of NO.

3.6. O_2-TPD and NO-TPD profiles of the BaO/Ce–Fe(x) catalysts

The O_2-TPD and NO-TPD profiles were examined to understand the reaction paths for the direct NO decomposition process. Fig. 8A shows the O_2-TPD profiles of the catalysts. For Ce–Fe(0) and Ce–Fe(0.02) without Ba loading, no desorption peak was observed, whereas the Ba-containing catalysts exhibited significant oxygen desorption peaks. The BaO/Ce–Fe(0) catalyst showed desorption peaks at ~340 ºC. Addition of a small amount of Fe caused a significant change in the O_2-TPD profile, and the

18

desorption peak shifted toward the lower temperature region. This result indicates that the desorption of oxygen is promoted by the addition of Fe to BaO/CeO_2. The amount of O_2 desorbed from the BaO/Ce–Fe(x) catalyst increased with increasing x to 0.02, but further increase in x decreased the amount (Fig. 8B). This trend is in good agreement with NO decomposition activity of the catalysts, indicating that the number of oxygen adsorption sites is correlated with the activity of the BaO/Ce–Fe(x) catalysts.

Fig. 9A shows NO-TPD profiles of BaO/Ce–Fe(x) catalysts after NO was adsorbed at 550 ºC. Desorption curves for N_2 and O_2 are also shown in the figure. Although the desorption of N_2 was not detected over the entire temperature range in the TPD process, immediate formation of N_2 was observed on the introduction of NO (NO adsorption process at 550 ºC). This feature was also observed for the BaO/Ce–Mn(x) catalysts [51]. All of the BaO/Ce–Fe(x) catalysts exhibited NO desorption peak at ~600 ºC, and O_2 desorption was also observed in the same temperature range. The ratios of O_2/NO desorbed from the catalysts were calculated to be 0.88 ± 0.05, indicating that surface nitrate species decomposed in this temperature range. The nitrate species was actually detected by the in-situ FT-IR spectra of the catalysts after NO adsorption, which showed a peak at 1294 cm^{-1} (data not shown). The amount of NO desorbed from the BaO/Ce–Fe(0.02) catalyst was larger than that desorbed from the other catalysts. This

result is in good accordance with the NO decomposition activity pattern. Since the NO

decomposition activity is correlated well with the oxygen vacancy concentration, the

amount of NO desorbed from the catalyst in the TPD experiment was plotted against the

I_{256}/I_{460} value (Fig. 9B). Linear correlation was obtained, suggesting that the oxygen

vacancy plays an important role for the formation of the surface nitrate species. Another

important point is that N–O bonds are easily cleft by the action of oxygen vacancies

yielding nitrogen and oxygen atoms. Although nitrogen molecules are easily desorbed

from the catalyst surface, the oxygen atoms react with NO molecules yielding surface

nitrate species. In other words, the oxygen atoms formed by decomposition of NO are

desorbed from the catalyst surface via surface nitrate species. This means that the

surface nitrate species is not an intermediate for the direct decomposition of NO but an

oxygen reservoir that interferes with the desorption of oxygen.

4. Conclusions

In the low Fe content region, CeO_2–Fe_2O_3 solid solutions with the CeO_2 cubic fluorite

structure are formed. The XANES spectra of the BaO/Ce–Fe(x) catalysts with low Fe

contents ($x < 0.048$) indicated that the local structure of iron had a tetrahedral

coordination environment. The ESR analysis indicated the presence of isolated Fe^{3+}

species in the catalysts. Incorporation of isolated tetrahedral Fe^{3+} in the fluorite structure of CeO_2 increased the concentration of oxygen vacancies. The maximum oxygen vacancy concentration was attained by the catalyst with the Fe content of 0.02 mol%, and further increase in the Fe content rather decreased the concentration of oxygen vacancies. The oxygen vacancy concentration directly correlated well with NO decomposition activity of the catalysts irrespective of the modifier (Fe or Mn) for the formation of the oxygen vacancies.

O_2-TPD profiles indicated that desorption of oxygen from the catalysts is promoted by Fe addition, and the largest amount of O_2 adsorption was observed for the BaO/Ce–Fe(0.02) catalyst. NO-TPD profiles showed that NO desorption was associated with the desorption of O_2, indicating that the oxygen atoms formed by decomposition of NO reacts with NO yielding surface nitrate species. This species is not an intermediate for the direct decomposition of NO but an oxygen reservoir that interferes with the desorption of oxygen.

performed at BL16B2 in SPring-8 with the approval of the Japan Synchrotron Radiation

Research Institute (JASRI) (Proposal No. 2010A5351).

References

[1] A. Trovarelli, Catal. Rev.-Sci. Eng. 38 (1996) 439–520.

[2] G. Neri, A. Pistone, C. Milone, S. Galvagno, Appl. Catal. B: Environ. 38 (2002) 321–329.

[3] Y. Kamimura, S. Sato, R. Takahashi, T. Sodesawa, T. Akashi, Appl. Catal. A: Gen. 252 (2003) 399–410.

[4] F.J. Pérez-Alonso, M.L. Granados, M. Ojeda, T. Herranz, S. Rojas, P. Terreros, J.L.G. Fierro, M. Gracia, J.R. Gancedo, J. Phys. Chem. B 110 (2006) 23870–23880.

[5] F.J. Pérez-Alonso, M.L. Granados, M. Ojeda, P. Terreros, S. Rojas, T. Herranz, J.L.G. Fierro, M. Gracia, J.R. Gancedo, Chem. Mater. 17 (2005) 2329–2339.

[6] M. Hrovat, J. Holc, S. Bernik, D. Makovec, Mater. Res. Bull. 33 (1998) 1175–1183.

[7] G.S. Li, R.L. Smith, H. Inomata, J. Am. Chem. Soc. 123 (2001) 11091–11092.

[8] A. Amirnazm, J.E. Benson, M. Boudart, J. Catal. 30 (1973) 55–65.

[9] E.R.S. Winter, J. Catal. 22 (1971) 158–170.

[10] M. Iwamoto, H. Yahiro, Y. Mine, S. Kagawa, Chem. Lett. 18 (1989) 213–216.

[11] M.A. Vannice, A.B. Walters, X. Zhang, J. Catal. 159 (1996) 119–126.

[12] S.B. Xie, M.P. Rosynek, J.H. Lunsford, J. Catal. 188 (1999) 24–31.

[13] M. Haneda, Y. Kintaichi, N. Bion, H. Hamada, Appl. Catal. B: Environ. 46 (2003)

473–482.

[14] Y. Teraoka, H. Fukuda, S. Kagawa, Chem. Lett. 19 (1990) 1–4.

[15] Y. Teraoka, T. Harada, S. Kagawa, J. Chem. Soc. Faraday Trans. 94 (1998)

1887–1891.

[16] T. Ishihara, M. Ando, K. Sada, K. Takiishi, K. Yamada, H. Nishiguchi, Y. Takita, J.

Catal. 220 (2003) 104–114.

[17] N. Imanaka, T. Masui, H. Masaki, Adv. Mater. 19 (2007) 3660–3663.

[18] H. Masaki, T. Masui, N. Imanaka, J. Alloy. Compd. 451 (2008) 406–409.

[19] S. Tsujimoto, K. Mima, T. Masui, N. Imanaka, Chem. Lett. 39 (2010) 456–457.

[20] K. Goto, H. Matsumoto, T. Ishihara, Top. Catal. 52 (2009) 1776–1780.

[21] S. Iwamoto, T. Yasuda, Y. Kouno, M. Inoue, Adv. Sci. Technol. 33 (2003) 375–380.

[22] S. Iwamoto, R. Takahashi, M. Inoue, Appl. Catal. B: Environ. 70 (2007) 146–150.

[23] W.-J. Hong, S. Iwamoto, M. Inoue, Catal. Lett. 135 (2010) 190–196.

[24] L.X. Chen, T. Liu, M.C. Thurnauer, R. Csencsits, T. Rajh, J. Phys. Chem. B 106

(2002) 8539–8546.

[25] B. Echchahed, A. Moen, D. Nicholson, L. Bonneviot, Chem. Mater. 9 (1997)

1716–1719.

[26] Y. Wang, Q.H. Zhang, T. Shishido, K. Takehira, J. Catal. 209 (2002) 186–196.

[27] G. Calas, J. Petiau, Solid State Commun. 48 (1983) 625–629.

[28] S. Bordiga, S. Coluccia, C. Lamberti, L. Marchese, A. Zecchina, F. Boscherini, F. Buffa, F. Genoni, G. Leofanti, G. Petrini, G. Vlaic, J. Phys. Chem. 98 (1994) 4125–4132.

[29] E. Abiaad, R. Bechara, J. Grimblot, A. Aboukais, Chem. Mater. 5 (1993) 793–797.

[30] A. Martínez-Arías, M. Fernández-García, C. Belver, J.C. Conesa, J. Soria, Catal. Lett. 65 (2000) 197–204.

[31] M.N. Timofeeva, S.Ts. Khankhasaeva, S.V. Badmaeva, A.L. Chuvilin, E.B. Burgina, A.B. Ayupov, V.N. Panchenko, A.V. Kulikova, Appl. Catal. B: Environ. 59 (2005) 243–248.

[32] A.V. Kucherov, M. Shelef, J. Catal. 195 (2000) 106–112.

[33] A. Parmaliana, F. Arena, F. Frusteri, A. Martínez-Arías, M.L. Granados, J.L.G. Fierro, Appl. Catal. A: Gen. 226 (2002) 163–174.

[34] M.S. Kumar, M. Schwidder, W. Grunert, A. Bruckner, J. Catal. 227 (2004) 384–397.

[35] L.P. Li, G.S. Li, R.L. Smith, H. Inomata, Chem. Mater. 12 (2000) 3705–3714.

[36] J. Pérez-Ramírez, M.S. Kumar, A. Brückner, J. Catal. 223 (2004) 13–27.

[37] D. Goldfarb, M. Bernardo, K.G. Strohmaier, D.E.W. Vaughan, H. Thomann, J. Am. Chem. Soc. 116 (1994) 6344–6353.

[38] A. Gervasini, C. Messi, P. Carniti, A. Ponti, N. Ravasio, F. Zaccheria, J. Catal. 262 (2009) 224–234.

[39] J. Pérez-Ramírez, F. Kapteijn, A. Brückner, J. Catal. 218 (2003) 234–238.

[40] S. Bordiga, R. Buzzoni, F. Geobaldo, C. Lamberti, E. Giamello, A. Zecchina, G. Leofanti, G. Petrini, G. Tozzola, G. Vlaic, J. Catal. 158 (1996) 486–501.

[41] J.R. McBride, K.C. Hass, B.D. Poindexter, W.H. Weber, J. Appl. Phys. 76 (1994) 2435–2441.

[42] B.M. Reddy, A. Khan, Catal. Surv. Asia 9 (2005) 155–171.

[43] F. Arena, G. Trunfio, J. Negro, B. Fazio, L. Spadaro, Chem. Mater. 19 (2007) 2269–2276.

[44] J. Kreisel, G. Lucazeau, H. Vincent, J. Solid State Chem. 137 (1998) 127–137.

[45] A. Nakajima, A. Yoshihara, M. Ishigame, Phys. Rev. B 50 (1994) 13297–13307.

[46] J.M. Gonzálezcalbet, S. Nicolopoulos, M. Valletregi, J. Less Common Met. 166 (1990) 343–352.

[47] H. Mitsuda, S. Mori, C. Okazaki, Acta Crystal. B 27 (1971) 1263–1269.

[48] R.C. Pullar, A.K. Bhattacharya, Mater. Lett. 57 (2002) 537-542–542.

[49] R.A. Candeia, M.A.F. Souza, M.I.B. Bernardi, S.C. Maestrelli, I.M.G. Santos, A.G. Souza, E. Longo, Ceram. Int. 33 (2007) 521–525.

[50] W.-J. Hong, S. Iwamoto, S. Hosokawa, K. Wada, H. Kanai, M. Inoue, J. Catal. 277 (2011) 208–216.

[51] W.-J. Hong, S. Iwamoto, M. Inoue, Catal. Today 164 (2011) 489–494.

Table 1. Compositions of the catalysts.

Sample	Bulk	Surface	
	Fe/(Ce+Fe)[a]	Fe/(Ce+Fe)[b]	Ba/(Ce+Fe+Ba)[b,c]
BaO/Ce-Fe(0)	–	–	0.24
BaO/Ce-Fe(0.01)	0.01	0.03	0.27
BaO/Ce-Fe(0.02)	0.02	0.06	0.27
BaO/Ce-Fe(0.048)	0.04	0.12	0.22
BaO/Ce-Fe(0.17)	0.13	0.25	0.18
BaO/Ce-Fe(0.5)	0.44	0.43	0.13
BaO/Ce-Fe(1.0)	1.00	1.00	0.21

[a] Molar ratio determined by ICP-AES analysis.
[b] Molar ratios determined by XPS.
[c] Nominal ratio of Ba/(Ce+Fe+Ba) for the catalysts is 0.06.

Table 2. Proportion of the area of each band obtained by deconvolution of the UV–vis spectra.

Catalyst	Fe_1[a]	Fe_2[b]	Fe_3[c]
	(%)	(%)	(%)
BaO/Ce–Fe(0.01)	11.5	88.5	—
BaO/Ce–Fe(0.02)	34.9	33.4	31.7
BaO/Ce–Fe(0.048)	14.9	46.2	38.9
BaO/Ce–Fe(0.17)	3.2	27.9	68.9
BaO/Ce–Fe(0.5)	1.1	19.6	79.3
BaO/Ce–Fe(1.0)	0.5	18.7	80.8

[a] Isolated Fe^{3+} ions.
[b] Oligomeric $Fe_x^{3+}O_y$ clusters.
[c] Large Fe_2O_3 particles.

Figure captions

Fig. 1. Fe K-edge XANES spectra of the BaO/Ce–Fe(x) catalysts. (a) $x = 0.01$, (b) $x = 0.02$, (c) $x = 0.048$, (d) $x = 0.17$, (e) $x = 0.5$, (f) $x = 1.0$, (g) α-Fe$_2$O$_3$, and (h) FePO$_4$.

Fig. 2. Proportion of tetrahedral Fe^{3+} in the BaO/Ce–Fe(x) catalysts calculated by the linear combination fitting analysis of the XANES spectra. For comparison, NO conversion at 800 °C and the mole of NO conversion (at 600 °C) normalized by mole of tetrahedral Fe^{3+} species are also plotted.

Fig. 3. ESR spectra of the BaO/Ce-Fe(x) catalysts measured at −196 °C: Magnetic field range: A, 50-550 mT; B, 300-380 mT; C, 120-200 mT. (a), $x = 0$; (b), $x = 0.01$; (c), $x = 0.02$; (d), $x = 0.048$; (e), $x = 0.17$; (f), $x = 0.5$; (g), $x = 1.0$; and (h), α-Fe$_2$O$_3$.

Fig. 4. UV–vis spectra of the BaO/Ce–Fe(x) catalysts. (a), $x = 0.01$; (b), $x = 0.02$; (c), $x = 0.048$; (d), $x = 0.17$; (e), $x = 0.5$; and (f), $x = 1.0$.

Fig. 5. Raman spectra of the BaO/Ce–Fe(x) catalysts (A), and expanded spectra (B): (a), Fe reference (α-Fe$_2$O$_3$); (b), $x = 1.0$; (c), $x = 0.5$; (d), $x = 0.17$; (e), $x = 0.048$; (f), $x =$

0.02; (g), $x = 0.01$; (h), $x = 0$: Raman spectrum of CeO_2 (Ce–Fe(0)) calcined at 800 °C is also given in (i).

Fig. 6. Dependence of the I_{256}/I_{460} value calculated from the Raman spectrum upon the composition of the BaO/Ce–Fe(x) catalyst. Correlation between I_{256}/I_{460} value and proportion of tetrahedral Fe^{3+} determined by the XANES spectra in shown in the inset.

Fig. 7. Correlation between NO conversion at 800 °C and the I_{256}/I_{460} value calculated from the Raman spectra of the BaO/Ce–Fe(x) (present study) and BaO/Ce–Mn(x) [51] catalysts.

Fig. 8. O_2-TPD profiles of the BaO/Ce–Fe(x) catalysts (A) and amount of O_2 desorbed from the catalyst (■) and the number of the desorbed oxygen atom per cerium atom (□) as well as the NO conversion activity at 800 °C (○) as a function of catalyst composition (B). (a), $x = 0$, (b) $x = 0.0.1$, (c) $x = 0.02$, (d) $x = 0.048$, (e) $x = 0.5$, (f) $x = 1.0$. O_2-TPD profiles of Ce–Fe(0.02) (g) and CeO_2 alone (Ce–Fe(0)) (h), both calcined at 800 °C, are also given.

Fig. 9. NO-TPD profiles of the BaO/Ce–Fe(x) catalysts (A) and correlation between amount of NO desorption and the I_{256}/I_{460} value (B). (a), $x = 0$; (b), $x = 0.01$; (c), $x = 0.02$; (d), $x = 0.048$; (e), $x = 0.17$.
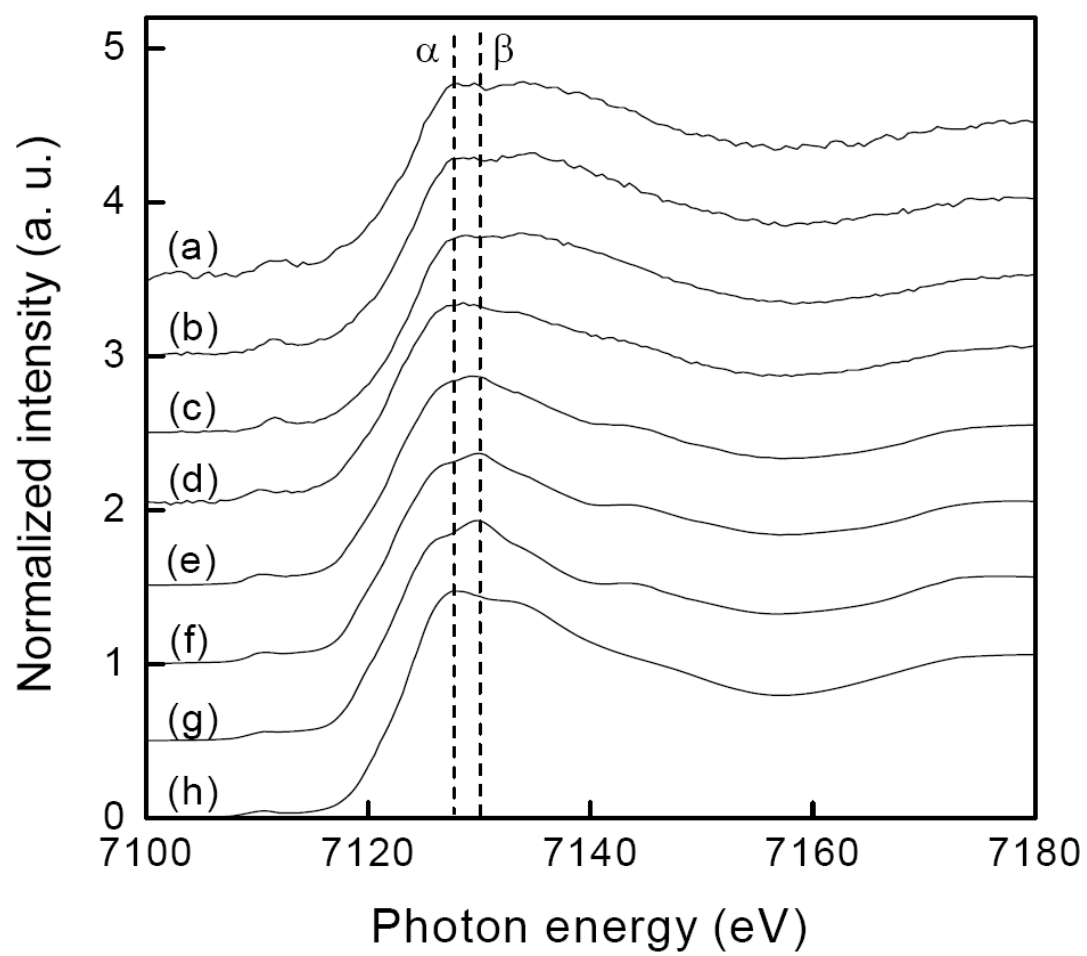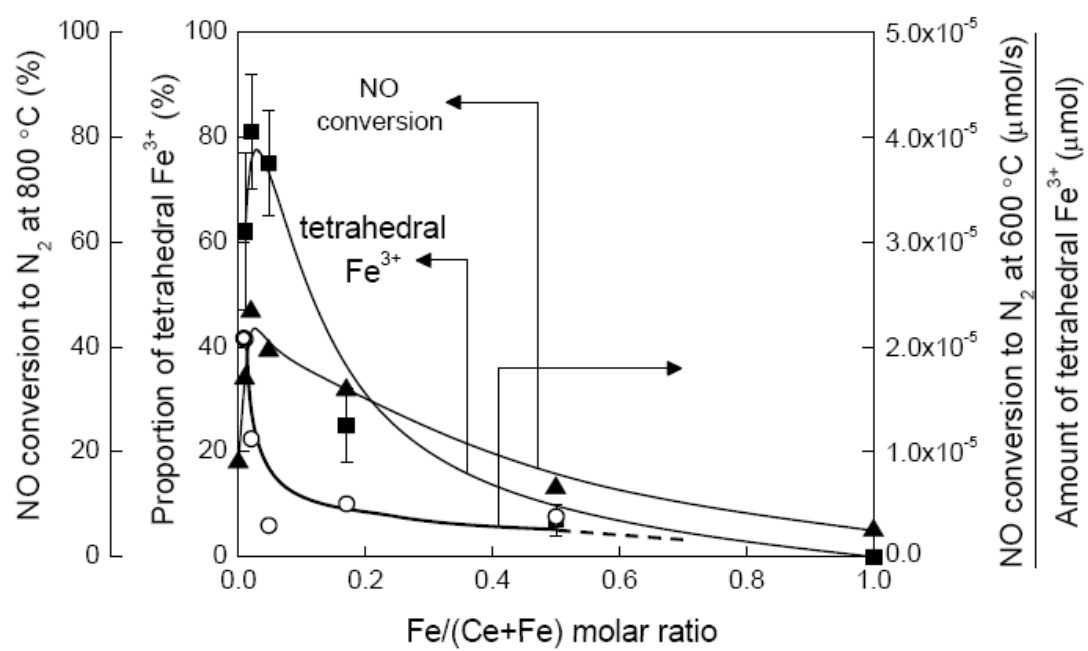
Fig. 1. W.-J. Hong et al.
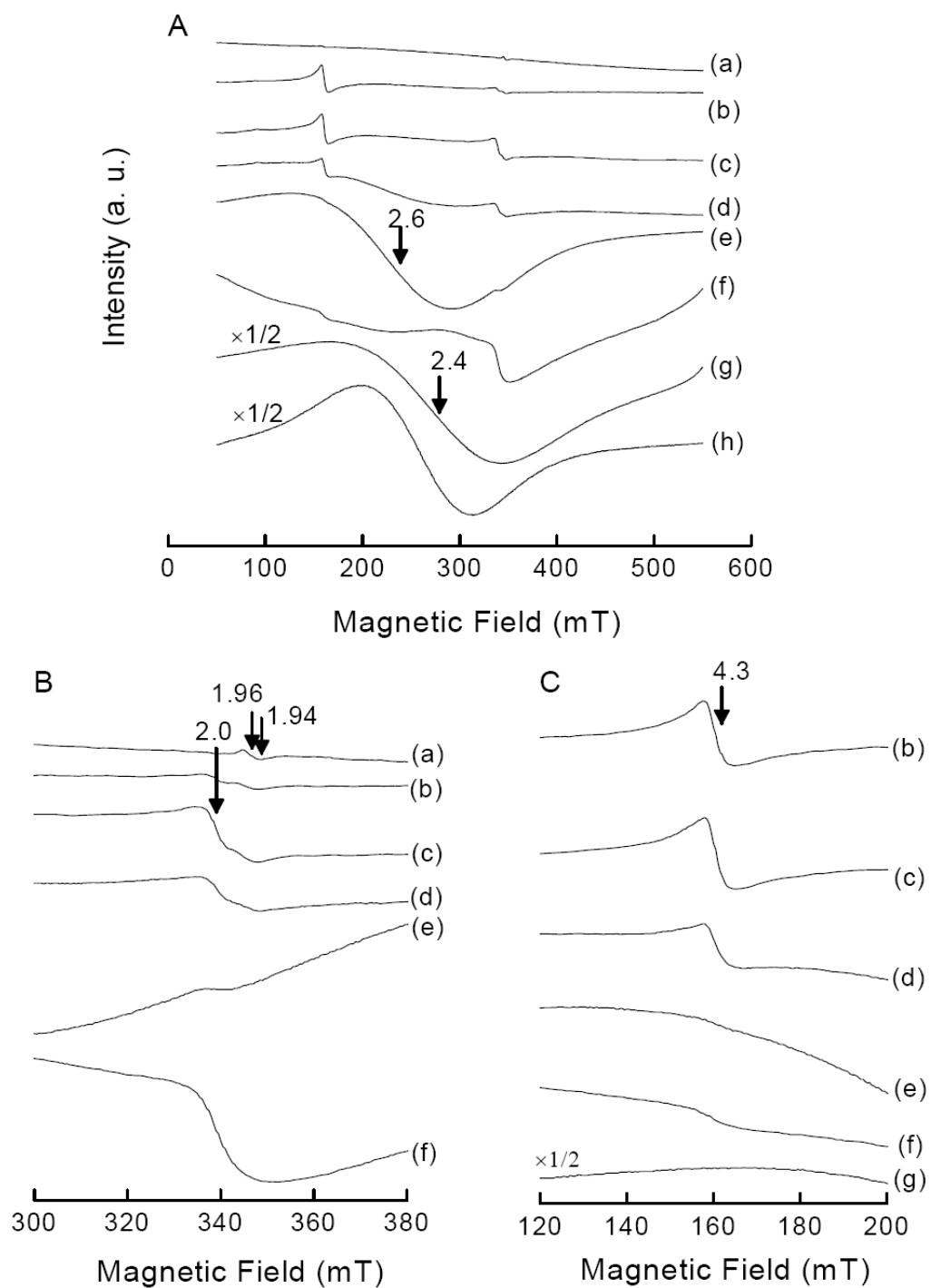
Fig. 2. W.-J. Hong et al.
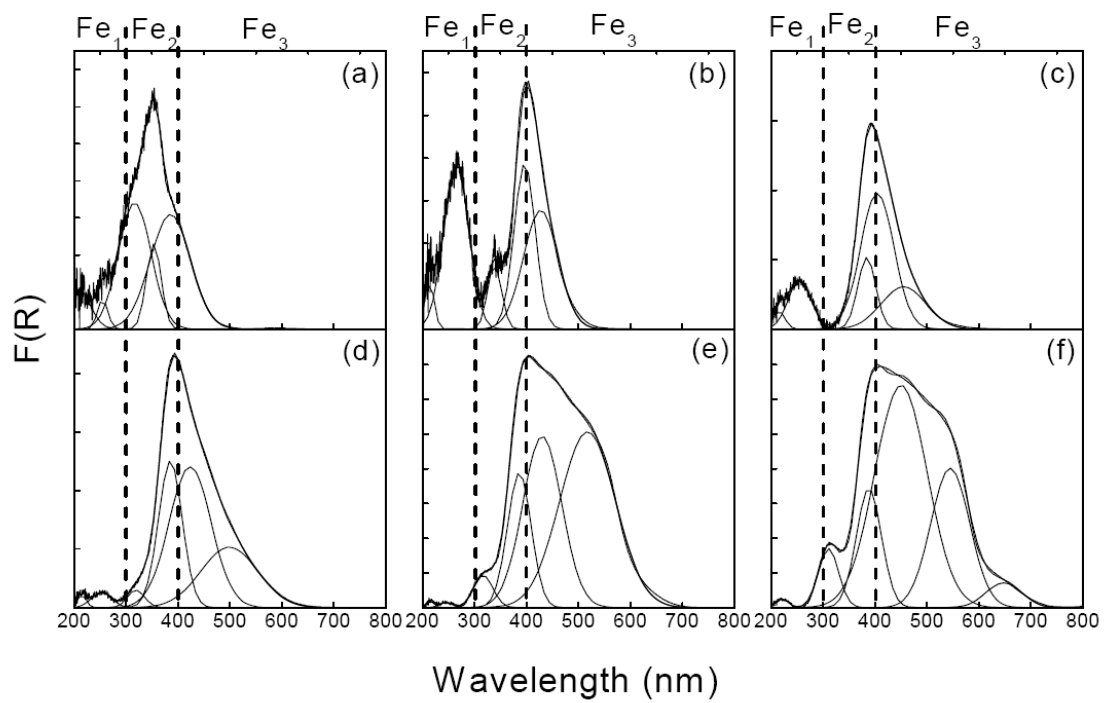
Fig. 3. W.-J. Hong et al.
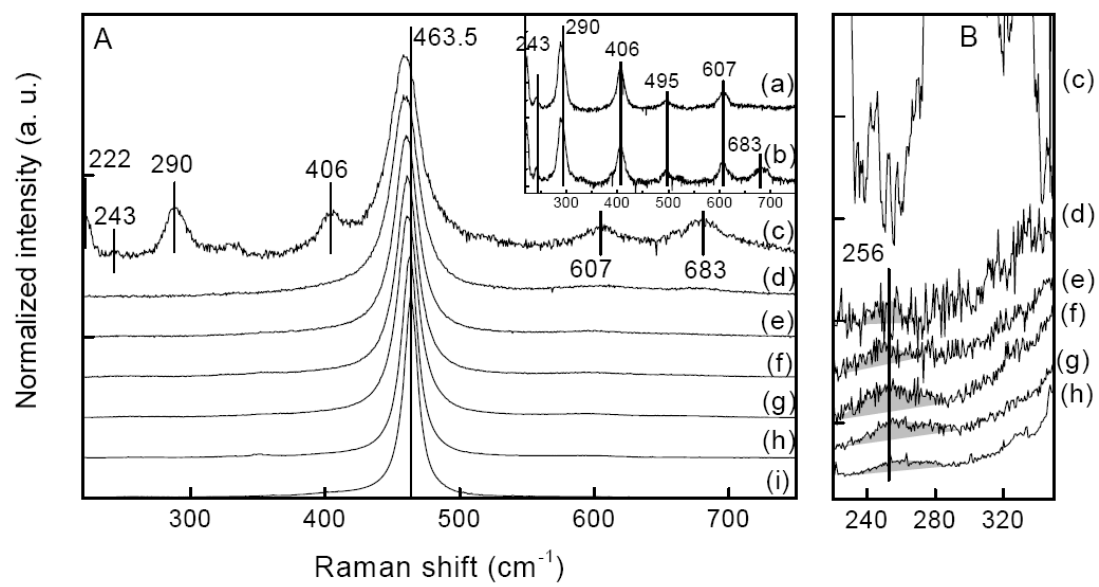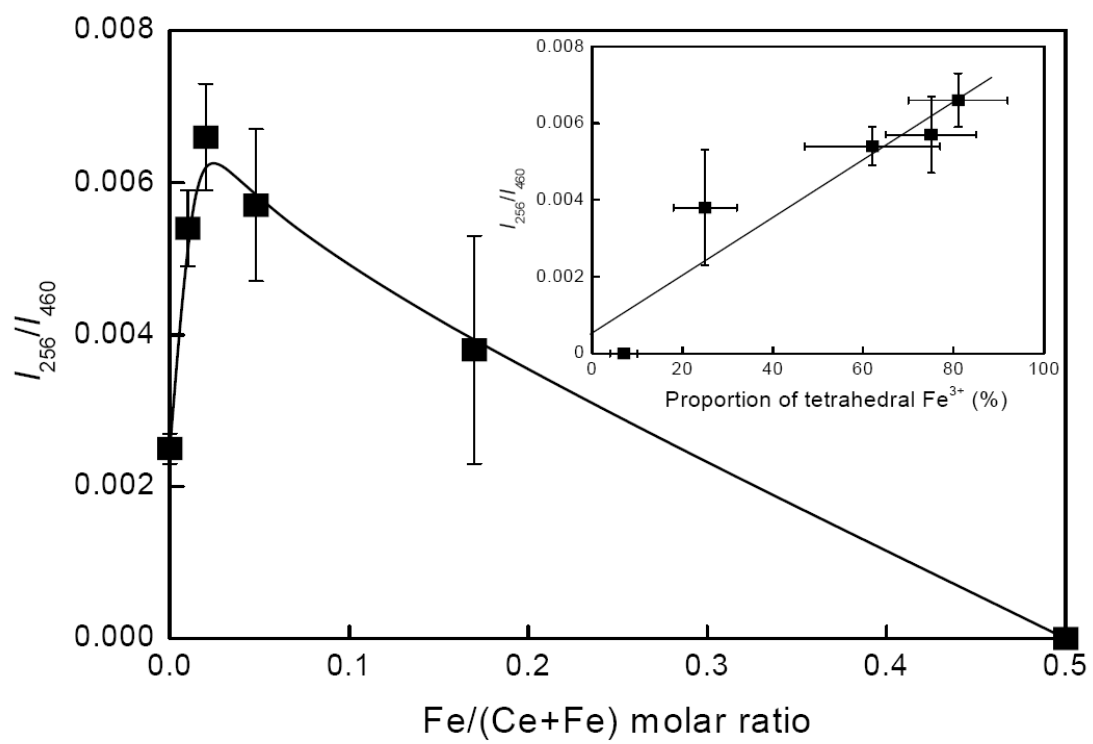
Fig. 4. W.-J. Hong et al.

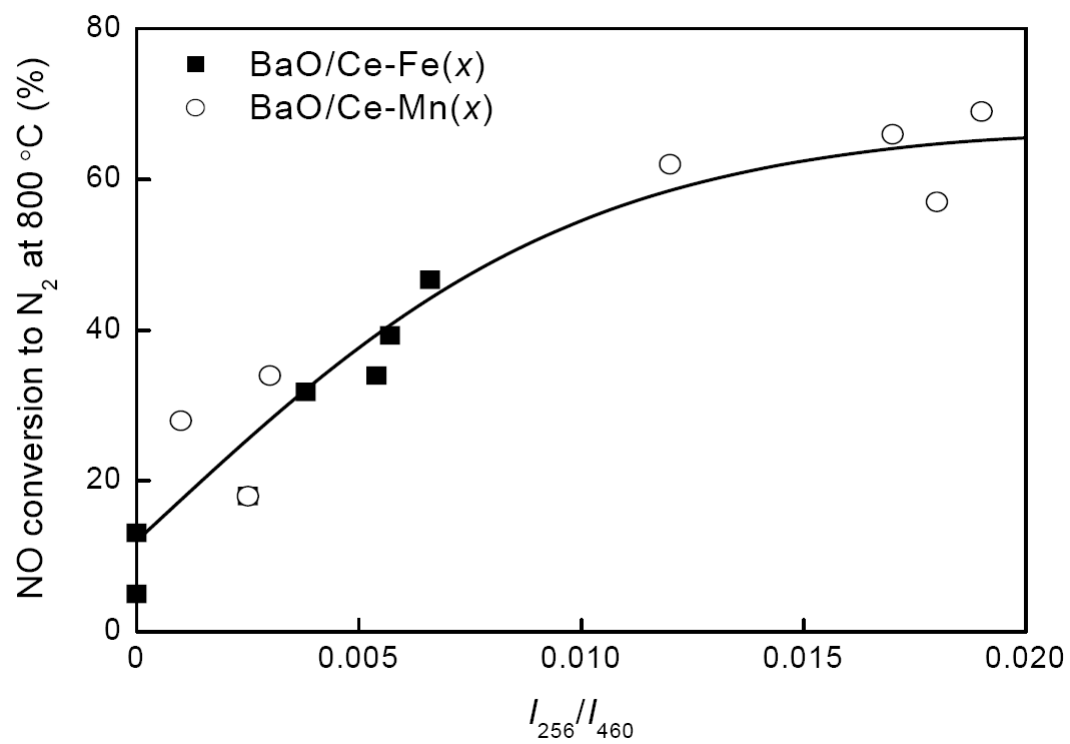Fig. 5. W.-J. Hong et al.
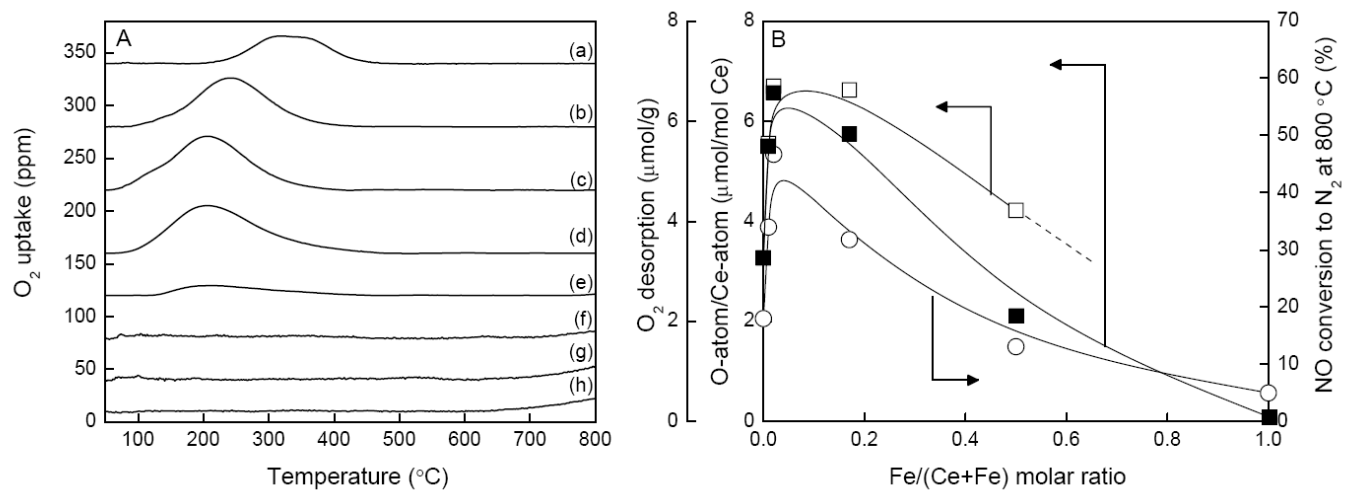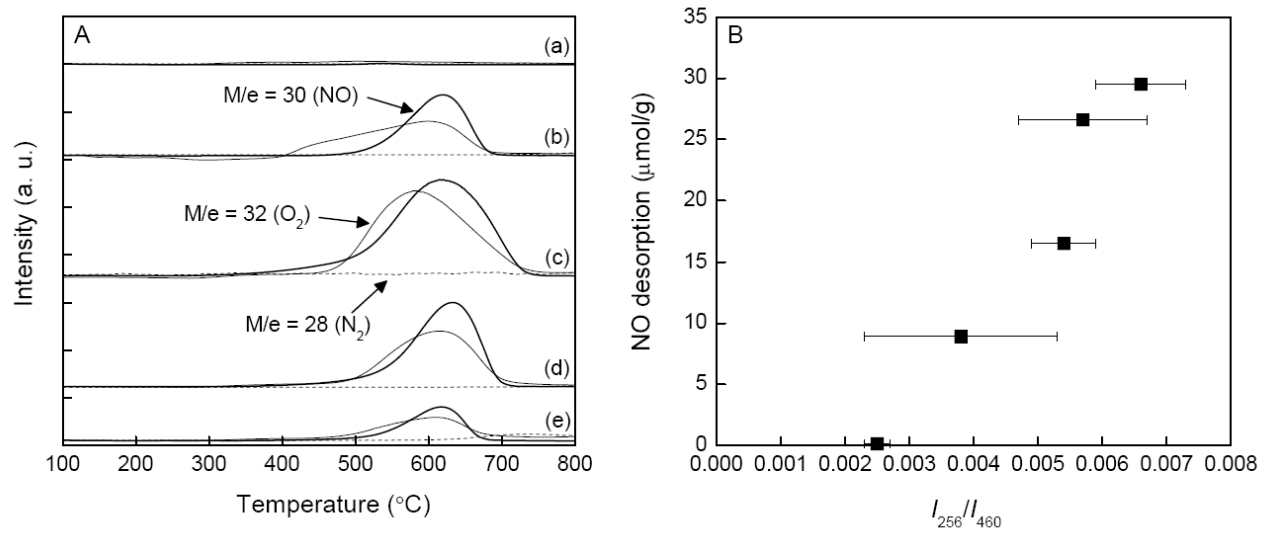
Fig. 6. W.-J. Hong et al.

Fig. 7. W.-J. Hong et al.

Fig. 8. W.-J. Hong et al.

Fig. 9. W.-J. Hong et al.